ADVANCED ENERGY MATERIALS
www.advenergymat.de

Organic-Additive-Derived Cathode Electrolyte Interphase Layer Mitigating Intertwined Chemical and Mechanical Degradation for Sulfide-Based Solid-State Batteries

Chanhyun Park, Juho Lee, Sangpyo Lee, Yu Jin Han, Jinsoo Kim, and Sung-Kyun Jung**

Keeping both the chemical and physical state of the electrode–electrolyte interface intact is one of the greatest challenges in achieving solid-state batteries (SSBs) with longer cycle lives. Herein, the use of organic electrolyte additives in the cathode electrolyte interphase (CEI) layer to mitigate the intertwined chemical and mechanical degradation in sulfide-based SSBs is demonstrated. Lithium difluorobis(oxalato)phosphate (LiDFBOP) and argyrodite (Li_6PS_5Cl) are used as a model system, with the LiDFBOP-derived CEI layer induced by irreversible oxidation above 4.12 V (vs Li^+/Li) during the formation cycle exhibiting dual functions. This CEI layer retards the rate of chemical degradation between the cathode active particles and solid electrolytes at high charging potential and helps maintain intimate physical contact even at a low stack pressure of 0.75 MPa. The improved physical contact enables delivery of a high initial capacity, while chemical stability suppressing the sulfite or sulfate formation has a more dominant effect on the long-term cycle stability. This study presents a new perspective and strategies for designing cathode coating materials for sulfide-based SSBs beyond the typically used inorganic oxide materials.

1. Introduction

In response to the ever-increasing demand for high energy density and safe energy storage devices, many efforts have focused on the development of rechargeable batteries and key component materials.[1,2] Many advances have been achieved in rechargeable battery materials, with solid electrolytes (SE) showing potential as alternatives to organic liquid electrolytes in terms of safety and the ability to use high-capacity anodes, such as lithium metal, thereby attracting interest in the realization of high-energy density solid-state batteries (SSBs).[3–8] Sulfide solid electrolytes are especially promising and advanced systems for industrial application owing to their high ionic conductivity (exceeding that of liquid electrolytes), high mechanical deformability, and low gravimetric density.[9–12] However, sulfide SEs suffer from chronic interfacial issues at the cathode–SE interfaces such as chemical degradation caused by side reactions due to the low oxidation stability of the S^{2-} anion[13–15] and a common issue of the mechanical contact loss between the cathode and SE due to the volume change of the cathode during galvanostatic cycling.[16–18]

Conventionally, oxide-based inorganic compounds with electronic-insulating and ionic-conducting character have been mainly proposed as the cathode coating layer to solely resolve cathode–SE chemical degradation.[19,20] Representatively, $LiNbO_3$ and Li_2ZrO_3 and their derivatives have been widely used and studied, with mitigated chemical degradation verified, suggesting improved cycle stability. However, the chemical-degradation-induced increase in the electronic resistance or diffusion of the cation in the cathode (i.e., Co for $LiCoO_2$) to the solid electrolyte is still not fully suppressed.[21–23] To design a coating material with better compatibility in both the oxide-based cathode and sulfide-based solid electrolyte, material screening with density functional theory (DFT) calculation has been attempted, considering further phase stability and electrochemical stability.[10,24] A few materials have been suggested within the set criteria; however, achieving uniform coverage of the materials with target composition and structure on the cathode is unexpectedly difficult given the monotonous application process of solid-state reaction at moderate temperature (300–500 °C) after solution-based precursor mixing and drying on the cathode surface.[25–27] Limiting the reaction temperature to exclude side reactions with the cathode material can instead induce discrepancies in the structure and composition from the target material; thus, it is difficult to achieve the original properties predicted from the DFT calculation. In addition, although the mechanical properties of the cathode coating layer have rarely been considered in the field of SSBs thus far, the high stiffness of oxide-based inorganic compounds could result in vulnerability to chemical degradation due to crack formation

C. Park, J. Lee, S. Lee, S.-K. Jung
Department of Energy Engineering
School of Energy and Chemical Engineering
Ulsan National Institute of Science and Technology (UNIST)
50 UNIST-gil, Ulsan 44919, Republic of Korea
E-mail: skjung@unist.ac.kr

J. Lee, Y. J. Han, J. Kim
Ulsan Advanced Energy Technology R&D Center
Korea Institute of Energy Research
25, Techno Saneop-ro 55beon-gil, Nam-gu, Ulsan 44776, Republic of Korea
E-mail: jkim@kier.re.kr

The ORCID identification number(s) for the author(s) of this article can be found under https://doi.org/10.1002/aenm.202203861.

DOI: 10.1002/aenm.202203861

resulting from anisotropic volume change of the cathode material.[10,28,29] A few nanometers coating layer inevitably suffer volume change due to the lower cohesive forces than forces induced by cathode expansion. In case of hard and brittle coating materials, such as $LiNbO_3$, the material can be fractured at the point contacts of cathode particles even in mechanical mixing with solid electrolyte during the electrode fabrication process.[30] The exposure of the newly generated surface to the solid electrolyte may accelerate chemical degradation by providing additional reaction sites. Therefore, the design and application strategies for cathode coating materials require further advancement, with current interests constrained to oxide-based inorganic compounds expanded to other material groups to improve the durability of SSBs.

Based on the criteria for cathode coating materials for SSBs, an organic-electrolyte-additive-derived cathode–electrolyte interphase (CEI) layer satisfies the ionic-conducting character including high chemical and electrochemical stability. These properties enable improved cycle retention even at high-voltage operation by securing an intact cathode surface in the lithium-ion battery (LIB) system.[31,32] Previously, phosphate and borate lithium salt additives with oxalate chemistry, such as lithium difluoro-bis(oxalato)phosphate (LiDFBOP),[33,34] lithium tetrafluoro-(oxalato)phosphate,[35] lithium difluoro-(oxalato)borate,[36,37] and lithium bis(oxalato) borate (LiBOB),[38–40] have been reported as CEI-layer-forming additives via oxidation reaction. In terms of mechanical properties, the CEI layer by oxidation of organic additive has similar Young's modulus to that of thiophosphate-based SE (E < = 20 GPa) in sharp contrast to the oxide coating layer with high Young's modulus such as $LiNbO_3$ (E = 195 GPa[41]) by having a value from 2.4 to 64.9 GPa.[42,43] Therefore, elastic deformation is expected to be more feasible than the conventional inorganic coating layer, effectively coping with the anisotropic volume change of the cathode materials.[30] In addition, organic-based additives can even effectively suppress microcracking of cathode materials by inducing homogeneous reactions with the formation of a uniform CEI layer.[44,45] Therefore, an organic-originated CEI layer can provide intuition to solve the complexly intertwined chemo-mechanical problems that can occur at the cathode–sulfide SE interface during high-voltage cycling. However, to date, the application of CEI-forming additives as a cathode protection layer in sulfide-based SSBs has barely been attempted.

Herein, by benchmarking the strategy, the feasibility of organic additives as cathode coating materials for sulfide-based SSBs is systematically investigated. The coating layer is applied by electrochemical oxidation of LiDFBOP, covering the cathode via a mechano-fusion method, under the formation cycle. Even a small amount of 0.3 wt% LiDFBOP coating effectively resulted in improved capacity at a low stack pressure of 0.75 MPa and longer cycle life with the dual function of mitigating chemical degradation and maintaining physical contact between the cathode and solid electrolyte. This organic-derived CEI layer provides insight to solve the chemo-mechanical problems that occur at the cathode–sulfide SE interface and suggests the feasibility of using organic materials as a coating material for SSBs beyond conventionally used oxide-based inorganic compounds.

2. Results and Discussion

2.1. Introduction of Organic Additive on Cathode Surface with Mechano-Fusion

The organic additive material is coated on the $LiNi_{0.6}Co_{0.2}Mn_{0.2}O_2$ (NCM) cathode surface by mechano-fusion principles with the shear force friction between the cathode and organic additive during the milling process in an air atmosphere (**Figure 1**). Organic additives are generally used by dissolving them in the liquid electrolyte in lithium-ion batteries; however, we introduce the additives as a protection layer directly for the cathode, aiming to generate an organic-based CEI layer during galvanostatic cycling. Phosphate-based LiDFBOP, known as a CEI-layer-forming additive in the LIB field, was coated on the NCM cathode surface as a model system to mitigate the interfacial degradation against an argyrodite electrolyte (Li_6PS_5Cl, LPSCl). The original particle size and morphological shape were retained even after the mechano-fusion milling process, as shown in the scanning electron microscopy (SEM) images (Figure S1a,b, Supporting Information). An amorphous protective layer with an optimized thickness of ≈5 nm with 0.3 wt% LiDFBOP additive was observed at the cathode surface in the transmission electron microscopy (TEM) images and fast Fourier transform (FFT) pattern, which shows a similar tendency to the 1.0 wt% LiDFBOP coating layer uniformly formed at about 20 nm on cathode surface (Figure 1a and Figure S2, Supporting Information). Uniform coverage of LiDFBOP was further elucidated with the electronic conductivity of cathode composite, which consists of cathode and SE. As shown in Figure S3 and Table S1, Supporting Information, composite cathode with bare NCM shows the highest electronic conductivity of 8.07×10^{-6} S/cm, followed by 0.3 wt% LiDFBOP mortar mixing (3.10×10^{-6} S cm^{-1}) and Nobilta milling NCM (2.82×10^{-7} S cm^{-1}). Simple addition, represented as mortar mixing of LiDFBOP, only shows a 61.5% decrease compared to bare NCM, however, NCM cathode covered by mechano-fusion method, represented as Nobilta milling, shows more than one order decrease in electronic conductivity. It implies that the mechano-fusion coating method ensures a uniform cathode surface coverage compared to simple hand mixing, thereby reducing the exposure of the active surface and exhibiting low electronic conductivity. In addition, energy-dispersive X-ray spectroscopy (EDS) mapping images showed an intensified signal from C and P atoms, corroborating the existence of the organic additive on the cathode surface, in contrast to the negligible signals for the bare NCM (Figure 1b,c). We verified the undamaged LiDFBOP coating material during the coating process by evaluating the thermal-decomposition behavior using thermogravimetric analysis (TGA). Upon heating from room temperature (RT) to 800 °C, noticeable weight loss was observed at approximately 90, 200, and 300 °C for LiDFBOP, as shown in Figure 1d. Analogous weight-loss behavior was also confirmed for a controlled sample of 1 wt% LiDFBOP-coated NCM (Figure 1e), and derivative peaks of the TGA curves indicating the decomposition temperature appeared at the same position as for the original LiDFBOP, indicating that the organic material was not deformed after mechano-fusion coating (Figure S4, Supporting Information). Considering that the LiDFBOP additive

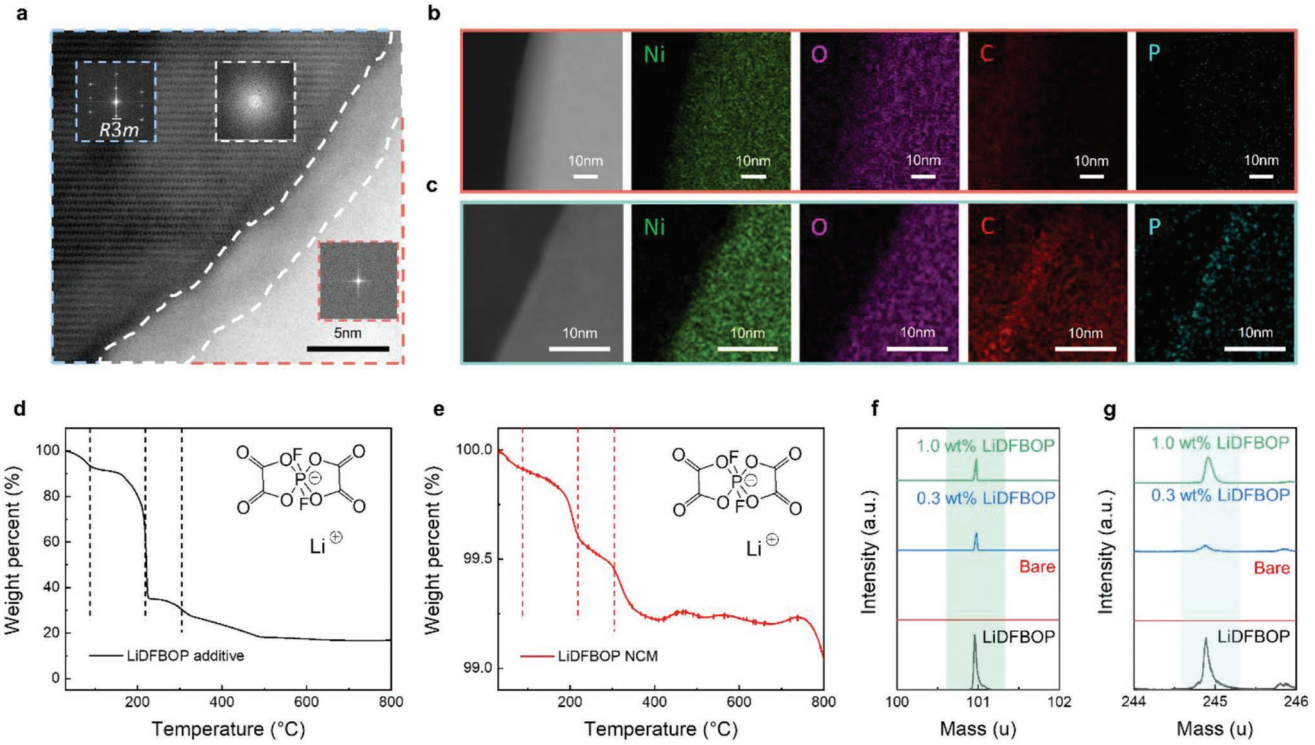

Figure 1. Introduction of the organic additive coating layer on the cathode surface with mechanofusion. a) STEM image of NCM surface coated with 0.3 wt% LiDFBOP. TEM and EDS mapping images for b) bare NCM and c) 0.3 wt%-LiDFBOP-coated NCM surface. TGA analysis of d) LiDFBOP additive and e) 1.0 wt%-LiDFBOP-coated NCM cathode. TOF-SIMS surface spectra of LiDFBOP additive, bare NCM, and LiDFBOP-coated NCM with different amounts of f) PO_4^- anion and g) $DFBOP^-$ anion.

underwent a total weight loss of 84% during heating up to 800 °C (in contrast to the negligible loss of below 0.2% for the bare NCM, Figure S5, Supporting Information), the weight loss of 0.9% for the 1 wt% LiDFBOP-coated NCM implies that the NCM cathode was covered by the additive with the target composition (Figure 1d,e). To determine the chemical composition of the coating layer, time-of-flight secondary ion mass spectrometry (ToF-SIMS) analysis was conducted (Figure 1f,g). Peaks corresponding to the phosphate anion (PO_4^-, ≈101 u) and difluoro-bis(oxalato)phosphate anion ($DFBOP^-$, ≈244.9 u) from the LiDFBOP additive were generated for both the 0.3 wt%- and 1.0 wt%-additive-coated cathode materials, whereas no signal was detected for the bare NCM cathode. Therefore, it is clear that the LiDFBOP additive adequately adhered to the NCM cathode surface without significant deformation of either the cathode or coating material during the mechano-fusion milling process.

2.2. Electrochemically Oxidized Organic Additive Mitigating Interfacial Chemical Degradation

The feasibility of the formation of the CEI layer induced by LiDFBOP oxidation in the sulfide-based SSB was first investigated. Given the limited amount of additives deposited on the NCM cathode, making it difficult to detect, galvanostatic cycling was conducted using only LPSCl and LiDFBOP compounds as a composite-cathode active material without the NCM cathode to verify the oxidation possibility of the LiDFBOP in SSB. The composite cathode, composed of LiDFBOP, LPSCl, and carbon nanofiber (CNF), showed irreversible oxidation by delivering a charge capacity of 36.6 mAh g^{-1} above 3.5 V (vs In/InLi), corresponding to 4.12 V (vs Li^+/Li); in contrast, negligible capacity was obtained by the composite cathode composed only of LPSCl and CNF (**Figure 2**a). This result indicates that the capacity at the first charge is delivered by oxidation of not the LPSCl but the LiDFBOP. It was confirmed that the additive composite exhibited a negligible capacity of 4 mAh g^{-1} for subsequent cycling after the initial oxidation reaction, which implies that the LiDFBOP additive was irreversibly oxidized during the galvanostatic cycling and can present as an oxidized CEI layer on the NCM cathode surface (Figure S6, Supporting Information). The P 2p and F 1s X-ray photoelectron spectroscopy (XPS) spectra for the additive composite cathode after oxidation indicated the formation of an oxidized CEI layer. As shown in Figure 2b,c, the emergence of new peaks corresponding to PO_3 (133.2 eV) and LiF (684 eV) was confirmed, indicating the composition of the CEI layer by comparing spectra showing one main peak of $Li_xPO_yF_z$ in P 2p (136 eV) and F 1s (686.8 eV) from the fresh LiDFBOP additive. In other words, the oxidation reaction of LiDFBOP generates a LiF and PO_3-based organic protective layer on the surface of the NCM cathode via the expected ring-opening reaction that has been suggested from chemically analogous additives such as lithium fluoromalonato(difluoro)borate (LiFMDFB), LiBOB, and LiDFBOP in previous reports with conventional liquid electrolyte system (Figure S7, Supporting Information).[45–47]

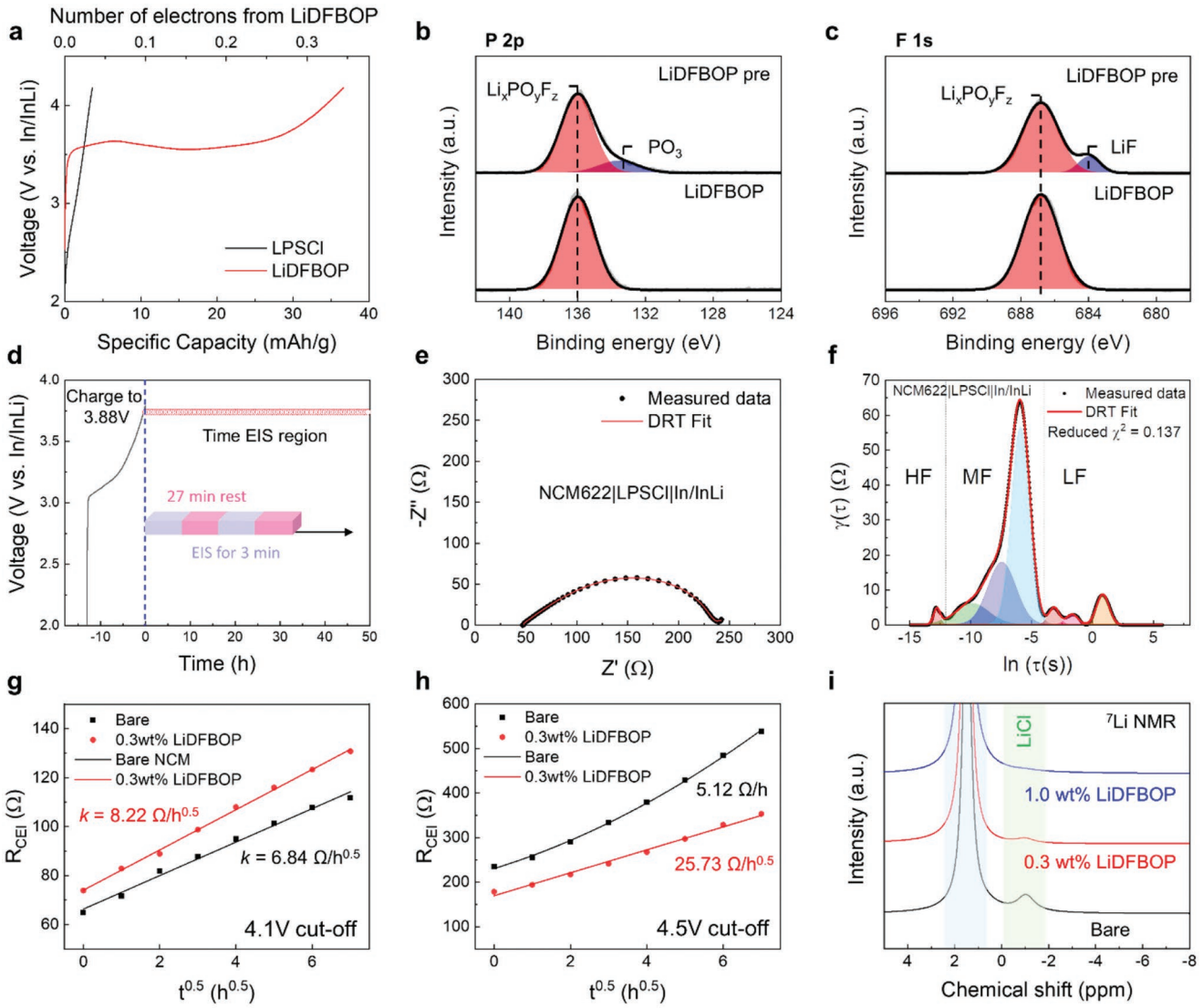

Figure 2. Electrochemical oxidation of LiDFBOP coating layer and its chemical stability. a) Voltage profiles of the initial cycle of LPSCl composite|LPSCl|In/InLi and LiDFBOP composite|LPSCl|In/InLi full cells. b) P 2p and c) F 1s XPS spectra of LiDFBOP additive and retrieved LiDFBOP composite after initial cycling of LiDFBOP composite|LPSCl|In/InLi full cell. Representative d) voltage profile, e) Nyquist plot, and f) DRT plot of an NCM composite|LPSCl|In/InLi full cell after charging up to 4.5 V (vs Li^+/Li). The linear and polynomial fits of CA|SE interface resistance, R_{CEI}, as a function of the square root of time ($t^{0.5}$) after charging up to g) 4.1 V (vs Li^+/Li) and h) 4.5 V (vs Li^+/Li). i) ^{7}Li solid NMR spectra of bare NCM, 0.3 wt% LiDFBOP, and 1.0 wt% LiDFBOP NCM composite after initial cycling between 2.5 and 4.5 V (vs Li^+/Li).

To investigate the chemical stability between NCM and LPSCl in the presence of the 0.3 wt% LiDFBOP coating layer, the impedance change as a function of time was measured over 50 h with a 27-min rest interval after charging up to a potential of 4.1 V and 4.5 V (vs Li^+/Li). The charging cut-off voltages were determined by considering the oxidation potential of LiDFBOP transforming into a CEI layer. Note that the impedance change for LiDFBOP-coated NCM at 4.1 V (vs Li^+/Li) indicates the stability of LiDFBOP itself against both LPSCl and NCM, whereas the impedance change at 4.5 V signifies the stability of the LiDFBOP-driven oxidized CEI layer. A representative first charging voltage profile up to 4.5 V (vs Li^+/Li) and an equivalent circuit model for electrochemical impedance spectroscopy (EIS) analysis are shown in Figure 2d and Figure S8, Supporting Information, respectively. The overall impedance gradually increased over time (Figures S9 and S10, Supporting Information), regardless of the coating layer. In the impedance analysis represented by the series connection of RC circuits, it is difficult to distinguish some elemental processes because of the overlap in the boundary frequency domain, indicating similar values of capacitance. To overcome this limitation, we used the distribution of relaxation times (DRT) method to effectively separate and investigate the ionic transport resistance in the grain boundary region of the cathode composite which is described to having a capacitance of 0.3 μF[48] (CA|CA), the cathode|SE interfacial resistance (CA|SE), and the anode|SE interfacial resistance (InLi|SE), which can be distinguishable at the high-, middle-, and low-frequency range, respectively.[17,49,50]

As shown in Figure 2e, the impedance spectrum obtained after 4.5 V charge perfectly fit with the DRT method, and each resistance component at high, middle, and low frequencies were separated as a function of relaxation time with a Gaussian function (Figure 2f). The impedance of the cell was majorly determined by the CA|SE interfacial resistance; therefore, the chemical degradation kinetics of the CA|SE interface against argyrodite (Li_6PS_5Cl) was systematically studied using the DRT method. The rate constants ($k_{CA|SE}$) were measured from the CA|SE interfacial resistance change obtained from the middle-frequency range as a function of the square root of time ($t^{0.5}$) before and after oxidative decomposition of the coating layer assuming the diffusion-controlled interphase growth model, as shown in Figure 2g,h.[51] The interfacial resistance of the CA|SE interface (R_{CEI}) follows the linear increase as a function of the square root of time according to Equation (1) by assuming that the charge transport is limited to ion diffusion across the interfacial layer, and each parameter is denoted in Table S2, Supporting Information.[52]

$$R_{CEI} = \frac{1}{S\overline{\sigma}_{CEI}}\sqrt{\frac{V_m}{xF^2}\cdot\frac{\overline{\sigma}_{Li^+}\cdot\overline{\sigma}_{e^-}}{\overline{\sigma}_{Li^+}+\overline{\sigma}_{e-}}\Delta\mu_{Li}}\cdot\sqrt{t} = \frac{1}{S\overline{\sigma}_{CEI}}\cdot k\sqrt{t} = k'\sqrt{t} \quad (1)$$

At a voltage of 4.1 V (vs Li^+/Li), where the oxidation of the LiDFBOP coating layer is suppressed, the bare NCM|SE interface and 0.3 wt% LiDFBOP NCM|SE interface showed comparable values of $k_{CA|SE}$, corresponding to 6.84 and 8.22 Ω $h^{-0.5}$, respectively (Figure 2g). Even the bare NCM|SE interface exhibited a slightly lower rate constant, which indicates that before the oxidation reaction, the LiDFBOP additive coating layer is ineffective in mitigating the chemical degradation with the sulfide SE at the CA|SE interface. However, the reverse trend was observed at high-voltage charging up to 4.5 V (vs Li^+/Li), where the irreversible oxidation of the LiDFBOP has already proceeded. After the oxidation reaction of LiDFBOP occurred above 4.1 V, the CA|SE resistance of 0.3 wt% LiDFBOP NCM exhibited sluggish degradation kinetics with a smaller slope of 25.73 Ω $h^{-0.5}$ in contrast to the bare NCM exhibiting a parabolic relationship with $t^{0.5}$ (Figure 2h). The parabolic increase of resistance for the bare NCM should be clarified through further research; however, it could result from the additional contribution of the chemical-reaction-induced physical contact loss between the cathode and solid electrolyte, as discussed in a previous report.[15] The tendency to show faster chemical degradation kinetics at higher potentials is consistent with the previously reported results at the interface between $Li_{10}GeP_2S_{12}$ and an NCM cathode,[52] and the overall resistance increase is expected to be dominant to the interfacial resistance increase as exposure time at high voltages (Figure S11, Supporting Information). Therefore, the introduction of the LiDFBOP coating layer, which has slower degradation kinetics at 4.5 V instead of 4.1 V compared with bare NCM, can substantially suppress the increase in resistance and ensure chemical stability at the CA|SE interface. To elucidate the mitigating effect on the chemical degradation of the LiDFBOP-oxidized CEI layer, we tracked the amount of LiCl as an indicator of chemical degradation using ^{7}Li solid-state nuclear magnetic resonance (NMR) after pre-cycling in the range of 2.5–4.5 V (vs Li^+/Li). The LiCl is known as a typical oxidation decomposition product of argyrodite including the Li_3PS_4, S.[53] In ^{7}Li solid-state NMR, the formation of LiCl was verified to be effectively repressed in the LiDFBOP-coated NCM after formation cycles compared with the bare NCM (Figure 2i). Even the amount of LiCl decreased as the amount of LiDFBOP covering the NCM surface increased. This finding corroborates the idea that the introduction of the oxidative organic coating layer can effectively suppress chemical degradation and insulate electron transport.

2.3. Additional Function Alleviating Mechanical Degradation at Cathode–Solid Electrolyte Interface

The transition of the resistance increase behavior as a function of the square root of time from a parabolic to a linear relationship when the LiDFBOP-derived CEI layer was adopted (Figure 2h) suggests the intriguing and radical notion that the organic additive coating layer can even mitigate the mechanical degradation at the CA|SE interface. The volume change of the layered cathode material (2–6%, until SOC 80) including asymmetrical lattice-parameter change during galvanostatic cycling[54] inevitably induces physical contact loss between the cathode material and SE in SSBs,[16,55] which was not considered in the conventional liquid-electrolyte system. To alleviate the mechanical degradation for securing the ionic and electronic percolation path in the cathode composite, high stack pressure (tens or hundreds of MPa) is generally applied in the operation of an SSB.[56–58] Therefore, to elucidate the function of the LiDFBOP-derived CEI layer in mitigating mechanical degradation, we investigated the cathode–solid electrolyte interfacial resistance change as the state of charge (SOC) at low stack pressure below 1 MPa (**Figure 3**a,b). At a low stack pressure of 0.75 MPa, a larger overpotential was observed at the bare NCM compared with the LiDFBOP-coated NCM, where more than 0.45 lithium was extracted from the NCM cathode (SOC 55). Because of the larger overpotential at the end of charge, the bare NCM delivered a capacity of 189.7 mAh g^{-1}, which was lower than that of the 0.3 wt%-LiDFBOP-coated NCM (201.1 mAh g^{-1}), as shown in Figure 3a. In addition, during the discharge process, the overpotential difference between the bare NCM and LiDFBOP-coated NCM was negligible except for at the end of discharge, and the LiDFBOP-coated NCM exhibited a larger discharge capacity (162.1 mAh g^{-1} for the 0.3 wt%-LiDFBOP-coated NCM versus 146.2 mAh g^{-1} for the bare NCM, as shown in Figure 3b). Note that the SOC that starts to increase the overpotential at the first charge is coincidentally consistent with the SOC that undergoes a drastic change in the unit-cell volume accompanying the elongation of the *c* lattice parameter and contraction of the *a* lattice parameter (Figure 3c and Figure S12, Supporting Information). Depending on the reversible capacity of the cathode, the volume change of the cathode particle appears differently. In order to clearly verify the physical deterioration at the interface against relatively similar SOC changes, the resistance change, and physical deterioration of the initial charge/discharge process are compared and analyzed under low stack pressure conditions maximizing interfacial mechanical degradation. As confirmed in the charging and discharging voltage profiles, a noticeable lower resistance of the LiDFBOP-coated NCM compared with that of

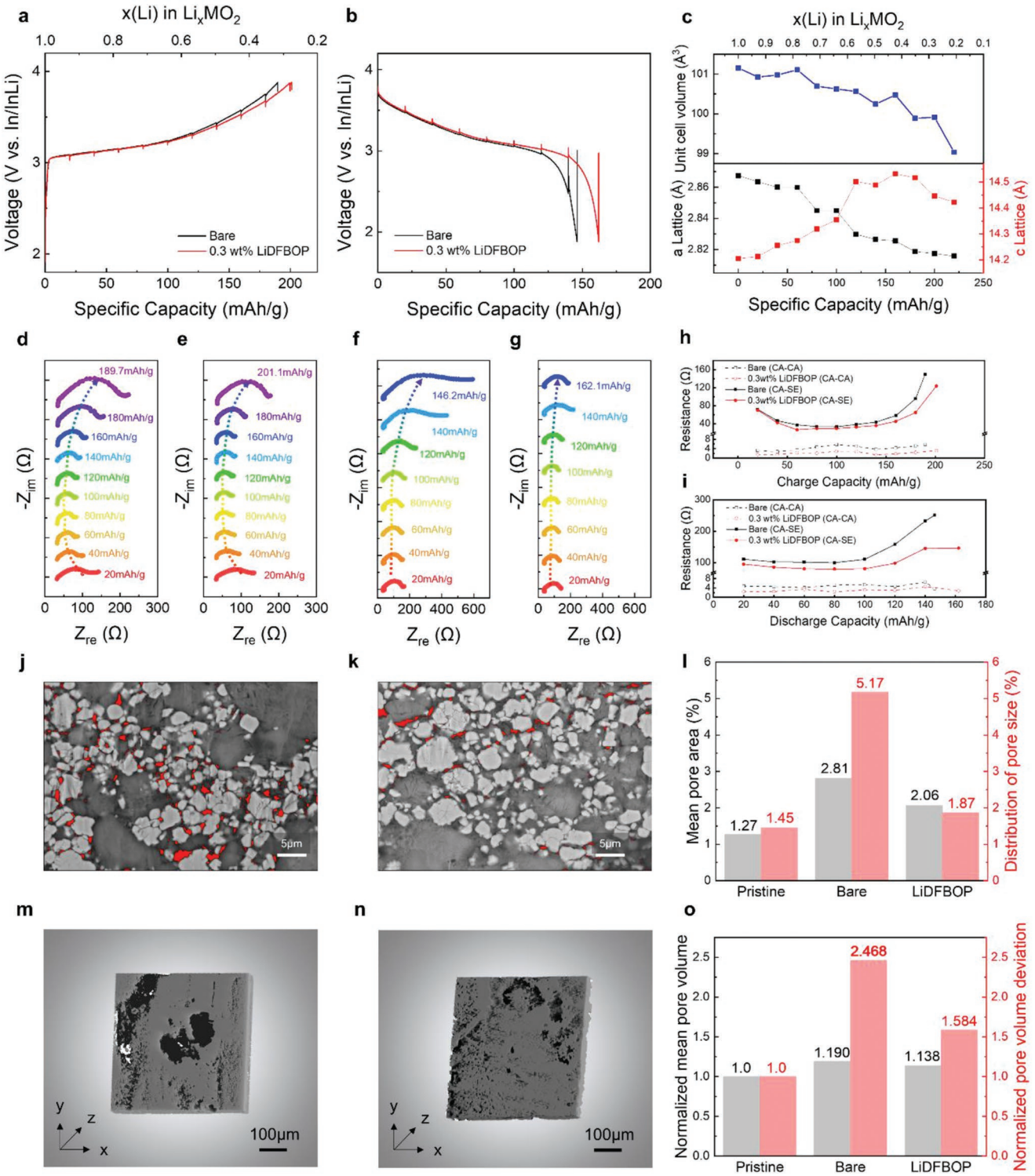

Figure 3. Mitigating effect on mechanical degradation of LiDFBOP-derived CEI layer. Initial a) charge and b) discharge profiles of bare NCM and 0.3 wt%-LiDFBOP-coated NCM under 0.75-MPa stack pressure within 2.5–4.5 V (vs Li^+/Li) at 25 °C and current densities of 0.15 mA cm^{-2} (corresponding to 20 mA g^{-1}). c) Unit-cell volume and lattice parameters (*a* and *c*) change according to SOC of NCM cathode. EIS spectra during d,e) charging with each 100 Ω main interval and f,g) discharging process with each 200 Ω main interval for bare NCM and 0.3 wt%-LiDFBOP-coated NCM, respectively. Comparison of cathode composite ionic transport and CA|SE interfacial resistance with every 20 mAh g^{-1} during h) charge and i) discharge. Cross-sectional SEM images of j) bare NCM composite and k) 0.3 wt%-LiDFBOP-coated NCM composite after initial cycling and corresponding l) mean pore area ratio and distribution of pore comparing with fresh cell and each cathode, SE, and pore were expressed in light gray, dark gray, and red color in cross-sectional SEM images. 3D X-ray CT images of the cathode composite consisted of cathode and SE for the m) bare NCM composite and n) 0.3 wt%-LiDFBOP-coated NCM composite after initial cycling and corresponding o) normalized mean pore volume and pore volume deviation ratio.

the bare NCM was clearly observed from above 120 mAh g^{-1} at both the first charge and discharge (Figure 3d–g). Please note that this resistance difference is noticeably increased at the end of discharge rather than the charging process. The increase of resistance differences at discharge is expected to be due to sluggish charge transfer kinetics at low SOC and mechanical degradation rather than chemical degradation, which will be discussed in detail later.[15] From the DRT analysis, the lower resistance of the LiDFBOP-coated NCM was confirmed to be majorly induced by the low CA|SE interfacial resistance (Figure 3h,i). The ionic transport resistance at the CA|CA interface was much lower than the CA|SE interfacial resistance; thus, its effect on the overall resistance was negligible; however, the LiDFBOP-coated NCM showed half the CA|CA resistance values compared with the bare NCM (Figure 3h,i). These results indicate that the LiDFBOP-derived CEI layer was effective in maintaining a lower resistance than the bare NCM even at low stack pressure by enhancing the ionic and charge transport at both the CA|CA and CA|SE interfaces. Given that the cell kinetics is determined by the charge-transport process at the CA|SE interface, the lower CA|SE resistance of LiDFBOP at the end of charge and discharge at low stack pressure could be due to enhanced charge-transfer kinetics affected by sluggish chemical degradation or mitigated constriction effect maintaining active surface area against contact loss. If the increase of the resistance at the end of the charge is mainly induced by chemical degradation, the difference in the interfacial resistance at the end of charging should be maintained or even increased during the discharge process due to the accumulation of the chemical degradation product. However, the large difference in overpotential or interfacial resistance between the bare and LiDFBOP-coated NCM observed at the end of charge (25.5 Ω) decreased at the beginning of discharge (15.4 Ω) and drastically increased at the end of discharge (Figure 3h,i). This result implies that the larger initial discharge capacity for the LiDFBOP-coated NCM (Figure 3b) could be majorly due to not the sluggish chemical degradation but the mitigated constriction effect. By assuming the exchange current density between the solid electrolyte and cathode increases as the SOC increases, similar to the effect between a liquid electrolyte and cathode,[59] the negligible difference at the beginning of discharge could be due to the high exchange current density compensating for the difference in the contact area of the cathode and solid electrolyte. However, at the end of discharge, the large difference in overpotential and interfacial resistance depending on the application of LiDFBOP can be represented by difference in the contact area, due to the low exchange current density. To further clarify the role of the LiDFBOP-derived CEI layer in mitigating mechanical degradation, cross-sectional SEM analysis on the cathode composites was performed after the initial cycling under low stack pressure (Figure 3j,k). The bare NCM composite cathode possessed a mean pore ratio of ≈2.8% with a mean area ratio of 62.5% for the SE and 34.7% for the cathode, whereas the 0.3 wt%-LiDFBOP-coated NCM composite cathode had a rather low mean pore area fraction of 2.1% with a mean area ratio of 63.5% for the SE and 34.4% for the cathode, compared to only 1.27% pore areas formed in fresh cells prior to electrochemical evaluation. (Figure 3l and Figure S13, Supporting Information). The difference in the pore fraction between the bare and LiDFBOP-coated NCM is due to the difference in the SE fraction and not the cathode fraction in the electrode, thus confirming that the difference in the pore fraction indicates the change in the contact area at the CA|SE interface. Please note that the absolute amounts or size of pores will be affected by the volume change of the cathode in the continuous electrochemical evaluation, therefore, this quantitative comparison for pore size or volume is valid between samples exhibiting similar charge or discharge capacity (ΔQ = 15.9 mAh g^{-1} for discharge between bare NCM and LiDFBOP coated NCM). In addition, the contrast of pores in the backscattered electron (BSE) image is affected by the height difference due to the various sizes of the 3D-formed pore volume during the analysis of the 2D destructive cross-section processing. Therefore, the deviation of the pore area fraction (Δr_p) expressed as the contrast difference can imply the distribution of the pore size, which could be an indicator that measuring the reaction uniformity among the cathode particles. A large deviation of the pore area fraction indicates an inhomogeneous volume change of the cathode, thus can imply a heterogeneous reaction in the composite cathode. The LiDFBOP-coated NCM maintains relatively uniform contact at the CA|SE interface (Δr_p = 1.87%), almost similar to that of a fresh cell (Δr_p = 1.45%), compared with the bare NCM (Δr_p = 5.17%) during charging and discharging under low stack pressure (Figure 3l and Figure S14a,b, Supporting Information). X-ray computed tomography (X-ray CT) analysis was conducted further for an in-depth understanding of contact intimacy between the cathode and SE in 3D space and to complement the destructive and 2D scale cross-sectional SEM analysis. Although micro-CT is inevitably hard to distinguish the solid electrolyte or cathode material including the Li element due to a very light element that interacts weakly with X-ray, it has the advantage of being able to analyze pores or voids in a non-destructive manner with a wide field of view (FOV) of several mm.[60] The X-ray CT image shown in Figure S15a, Supporting Information indicates that the SE layer and the cathode composite layer are presented at a thickness of 527 and 82 μm, respectively. The NCM cathode and SE are marked with gray color, and the empty spaces with pores are shaded with a black color for the distinct reminder of pores (Figure S15b, Supporting Information). The large volume of measurement (500 × 500 × 60 μm) can overcome the spatially limited analysis to a specific area, therefore, represents the pore volume and pore size distribution in composite cathode more accurately. The physical contact enhancement effect of the CEI layer derived from LiDFBOP was also verified in X-ray CT after initial cycling under low stack pressure conditions likewise SEM analysis (Figure 3m,n). Also, as shown in Figure S16, Supporting Information, more extreme formation and distribution of pores are observed with bare NCM. Although bare NCM exhibits a large size and pore distribution, LiDFBOP-coated NCM clearly shows a comparably small size and pore distribution after initial cycling. As shown in Figure 3o, compared to the pristine cathode composite, the bare NCM shows a mean pore volume increased by 19.0%, whereas the LiDFBOP-coated NCM provides a somewhat lower mean pore volume increment of 13.8% after initial cycling. In addition, bare NCM showed a significant pore volume deviation of 146.8% increase compared to pristine cathode composite,

however, LiDFBOP-coated NCM showed only a 58.4% increase, which means that the introduction of LiDFBOP-derived CEI layer on cathode surface can enhance the reaction uniformity of each cathode particle and alleviate the interfacial delamination of SE from the NCM cathode. This finding suggests that the LiDFBOP-derived CEI layer consequently facilitates the interparticle homogeneous reaction in the composite electrode with uniform and intimate contact, which may explain the higher discharge capacity.

2.4. Enhanced Electrochemical Performance

The effect of the dual function of the LiDFBOP coating layer in mitigating chemical and mechanical degradation of the electrochemical performance was investigated. To elucidate the effect of the LiDFBOP-derived CEI layer, the electrochemical properties of the bare NCM and 0.3 wt% LiDFBOP NCM were compared under high-voltage conditions where the deterioration at the cathode–SE interface was severe (up to 4.5 V vs Li^+/Li) in terms of both chemical and mechanical degradation. **Figure 4**a shows that bare NCM and 0.3 wt% LiDFBOP-coated NCM delivered similar charge capacities of 208.8 and 216.1 mAh g^{-1}, respectively. However, after the first charge, the 0.3 wt% LiDFBOP NCM exhibited a relatively high initial coulombic efficiency of 79.1%, whereas the bare NCM exhibited a lower value of 74.2%. The difference in cell degradation of the NCM cathode after the first cycle was also confirmed by voltage hysteresis in subsequent cycling. As shown in Figure 4b,c, the LiDFBOP additive coating layer showed lower voltage hysteresis in the 0.3 wt% LiDFBOP NCM ($\Delta V = 0.18$ V) compared with the bare NCM ($\Delta V = 0.23$ V) because of the ensured interfacial stability. The 0.3 wt%-LiDFBOP-coated NCM exhibited enhanced capacity retention of 79.7% at C/4 (1 C = 1.32 mA cm^{-2}) after 100 cycles with initially higher discharge capacity (148.3 mAh g^{-1}) compared with the 44.5% capacity retention of the bare NCM with lower initial capacity (112.9 mAh g^{-1}) (Figure 4d). The adoption of the 0.3 wt% LiDFBOP on the NCM surface also led to the improvement of the high-rate properties, as shown in Figure 4e. Note that the oxidation reaction of LiDFBOP can result in the formation of a PO_3-based organic layer and a LiF-based inorganic layer at the interface (Figure 2b,c). To clarify the origin of the enhanced interfacial and electrochemical properties, we investigated the effect of the inorganic LiF film separately using an NCM cathode covered by 0.3 wt% of LiF surface using the same mechano-fusion protocol. Because LiF is the most stable compound having the widest electrochemical stability window,[13] improved electrochemical properties were expected; however, the 0.3 wt% LiF-coated NCM exhibited nearly identical initial voltage profile, discharge capacity, and capacity retention as the bare NCM under C/10 charge/discharge condition (Figure S17, Supporting Information). In addition, increasing the initial charge cut-off from 4.5 V (vs Li^+/Li) to 4.8 V (vs Li^+/Li) to further promote the oxidation reaction

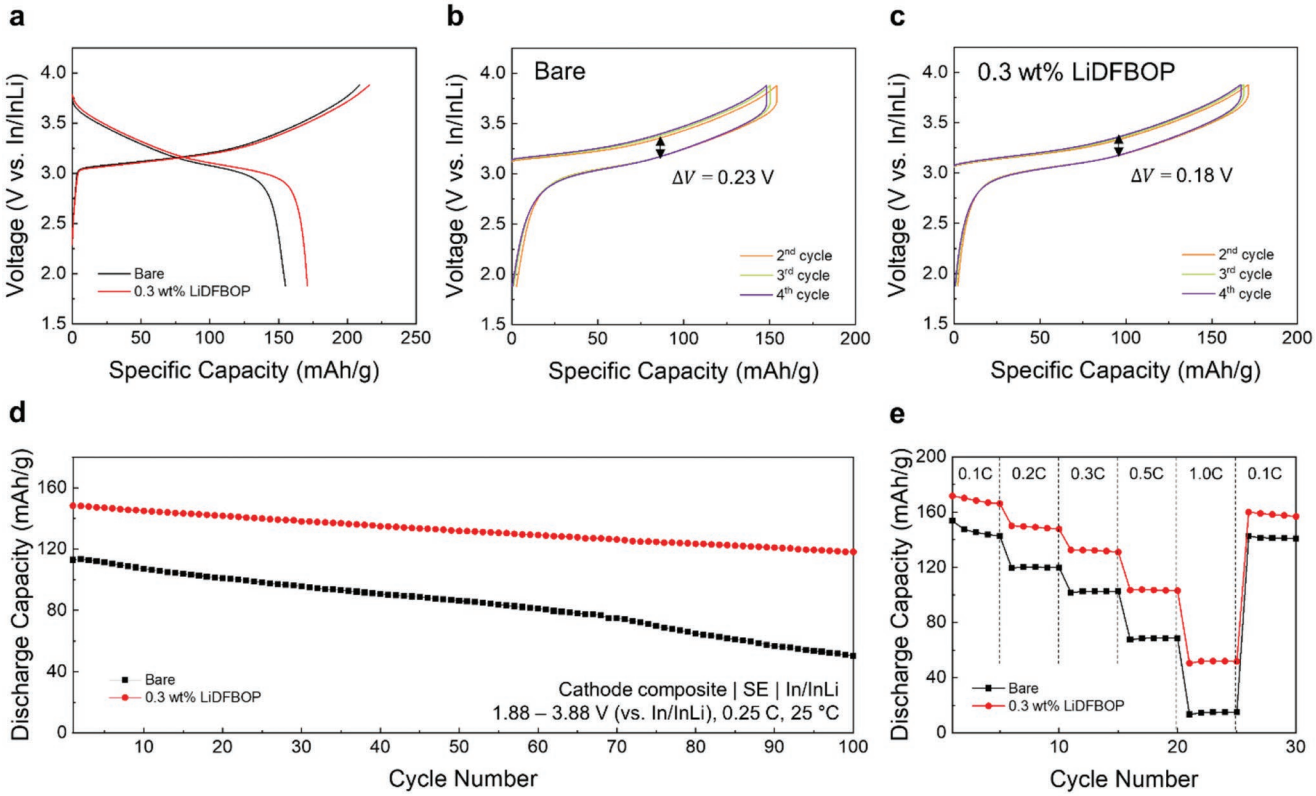

Figure 4. Effect of LiDFBOP coating layer on electrochemical performance. a) Voltage profiles of the initial cycle of NCM composite|LPSCl|In/InLi with bare NCM and 0.3 wt%-LiDFBOP-coated NCM at 25 °C at C/10. Subsequent voltage profiles of b) bare NCM and c) 0.3 wt%-LiDFBOP-coated NCM. d) Comparison of long-term cycle performance between bare NCM and 0.3 wt%-LiDFBOP-coated NCM at C/4. e) Rate capability of bare NCM and 0.3 wt%-LiDFBOP-coated NCM at different C-rates.

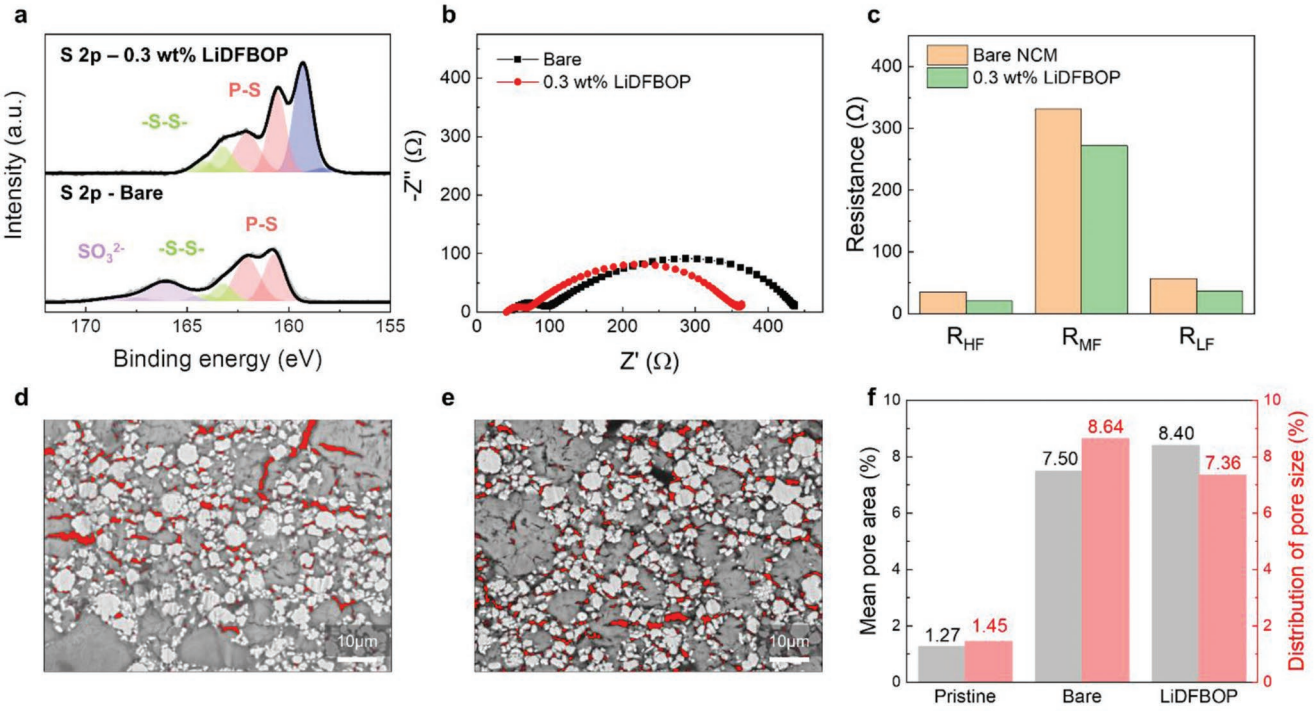

Figure 5. Post-mortem analysis of degradation mechanism. a) S 2p XPS spectra of bare NCM and 0.3 wt%-LiDFBOP-coated NCM after 100 cycles. b) Impedance spectra and c) corresponding resistances for each frequency range of the bare NCM and 0.3 wt%-LiDFBOP-coated NCM at 100th charge. Cross-sectional SEM images of d) bare NCM and e) 0.3 wt%-LiDFBOP-coated NCM after 100 cycles. f) Comparison of mean pore area ratio and pore size distribution of between bare and 0.3 wt%-LiDFBOP-coated NCM comparing with fresh cell after 100 cycles in a fixed cathode area fraction.

of LiDFBOP increases the organic PO_3 fraction and improves the electrochemical performance (Figure S18, Supporting Information). This result indicates that the LiF film produced by the oxidation of LiDFBOP had a negligible effect, and the PO_3-moiety-based organic interfacial film rather ensures (electro) chemical stability against highly reactive SE and alleviated physical contact loss at the CA|SE interface.

2.5. Post-Mortem Analysis on Degradation Mechanism

For an in-depth understanding of the degradation mechanism of the SSB, we performed post-mortem analysis after 100 cycles on both the chemical and mechanical deterioration at the cathode interface. First, we investigated the chemical degradation products using XPS, as shown in **Figure 5**a. The S 2p XPS spectra for the cycled cathode composites showed an increase in the intensity of sulfite SO_3^{2-} moiety for the cycled bare NCM which is a typically observed signal resulting from the vigorous oxygen-involved reaction between the cathode and SE at high voltage (Figure 5a).[61,62] However, the 0.3 wt% LiDFBOP-coated NCM exhibits the absence of SO_3^{2-} signal (Figure 5a), which indicates that the oxidized LiDFBOP effectively precluded the direct reaction between the cathode and SE during long-term cycling. Instead, new sulfur binding (≈159 eV) expected to be associated with the chemical bonding between argyrodite and the oxidized form of LiDFBOP formed at the interface appeared, which is expected to subdue the chemical degradation reaction between the NCM cathode and argyrodite electrolyte. The lower interfacial resistance was also confirmed for the 0.3 wt% LiDFBOP-coated NCM in the impedance spectra of the charged state after the 100th cycle (Figure 5b). The 0.3 wt% LiDFBOP-coated NCM exhibited lower cathode ionic transport resistance and CA|SE and InLi|SE interface resistance compared with that of the bare NCM, with corresponding values of 14.9, 59.3, and 20.7 Ω, respectively (Figure 5c). Although the CA|SE interfacial resistance majorly contributed to reducing the overall resistance for the LiDFBOP-coated NCM, both the CA|CA ionic transport and InLi/SE interfacial resistance also played considerable roles, and the suppressed increase in both resistances may be subordinate to the LiDFBOP-coating effect. As confirmed in the low-stack-pressure experiment, the relatively high uniformity of the pore size can lead to a homogeneous cathode reaction within the electrode, and it may have helped to maintain a uniform ionic transport pathway at the CA|CA interface during long-term cycling. In addition, because the non-uniformity of the reaction in the cathode can lead to reaction heterogeneity at the anode/SE interface according to a recent report,[63] the larger anode/SE interfacial resistance of the bare NCM may be the result of cross-talk caused by the reaction heterogeneity at the cathode side.

Second, X-ray CT and cross-sectional SEM analysis were performed after the long-term cycling to compare the mechanical deterioration caused by the repeated volume change of the NCM cathode. After the initial 50 cycles, 0.3 wt%-LiDFBOP-coated NCM shows a lower normalized pore volume of 0.154 and a lower normalized pore distribution of 1.169 compared to bare NCM in X-ray CT (Figures S19 and S20,

Supporting Information). As shown in the SEM BSE images (Figure S21, Supporting Information), the cycled electrode with the LiDFBOP-coated NCM appeared to have a larger fraction of pores compared with the electrode with the bare NCM. In terms of the pore size and distribution, physical contact loss occurred more uniformly after cycling for the 0.3 wt% LiDFBOP-coated NCM, whereas the pore size and distribution appeared to be heterogeneous for the cycled bare NCM (Figure 5d,e). These features were quantitatively confirmed by image analysis, as shown in Figure 5f. Both the bare NCM and 0.3 wt% LiDFBOP-coated NCM cycled cathode showed a large area fraction of pores of over 7%, and the LiDFBOP-coated NCM cathode exhibited a considerably larger mean fraction of pores (8.4%) than the bare NCM (7.5%) after cycling. The more significant mechanical deterioration of the LiDFBOP-coated NCM than the bare NCM is believed to result from the higher reversible capacity accompanied by inevitably larger volume change and accumulated stress during cycling, as discussed in Figure 3c. Please note that reversible capacity is higher for 0.3 wt%-LiDFBOP-coated NCM than bare NCM on the basis of SOC 55 that suffers a large anisotropic change in lattice parameters (ΔQ = 35.4 mAh g^{-1} for discharge between bare NCM and LiDFBOP coated NCM). The 0.3 wt%-LiDFBOP-coated NCM exhibits a higher discharge capacity than 124.7 mAh g^{-1} (SOC 55) up to 75 cycles with a high initial discharge capacity of 148.3 mAh g^{-1} (SOC 46) compared to only 112.9 mAh g^{-1} (SOC 60) initial discharge capacity of bare NCM. Therefore, 0.3 wt%-LiDFBOP-coated NCM is inevitable for accumulated larger volume change than bare NCM, which could lead to a larger mean fraction of pores. For the pore size distribution, the bare NCM (Δr_p = 8.64%) showed a more heterogeneous distribution than the LiDFBOP-coated NCM (Δr_p = 7.36%) even after cycling, which indicates that the bare NCM may undergo a more inhomogeneous reaction during cycling. Although the mechanical degradation was more severe for the 0.3 wt% LiDFBOP NCM than for the bare NCM, higher capacity and retention were achieved during long-term cycling; therefore, it implies that the complex understanding of cycle degradation mechanism by considering multiple deteriorating factors is required, including chemical and mechanical degradation during cycling. In detail, mechanical degradation can be largely expressed by two factors, the absolute amount of formation of physical pores and the uniformity of pore size in the composite cathode. First, the absolute amounts of pores will be affected by the volume change of the cathode in the continuous electrochemical cycling, which means that the reversible capacity of the cathode affects the amount of entire pore formation. Second, the distribution of pores could be determined by the reaction uniformity between the cathode particles, which is expressed differently depending on the homogeneity of chemical degradation related to the thickness or degradation product at each cathode particle interface. In this respect, mechanical degradation and chemical degradation is believed to be intertwined with each other. As shown in **Figure 6**, the introduction of a chemically stable organic-based CEI layer leads to a uniform volume change at the cathode particles, resulting in improved pore formation uniformity. Meanwhile, chemically vulnerable bare NCM could inevitably suffer an inhomogeneous reaction in the cathode particle ensemble leading to heterogeneous pore size distribution and mechanical degradation. Therefore, a high reversible capacity of LiDFBOP-coated NCM during the galvanostatic cycling induces increments in the absolute contact loss in the cathode composite, however, the distribution of the pores was relatively low (Figure 5f) compared to bare NCM. It is due to the organic-based homogeneous CEI layer alleviating the chemical degradation at the interface and improvement on the reaction uniformity between the NCM cathode particles. In other words, it means that chemical degradation should be considered and suppressed antecedently to improve long-term cycle

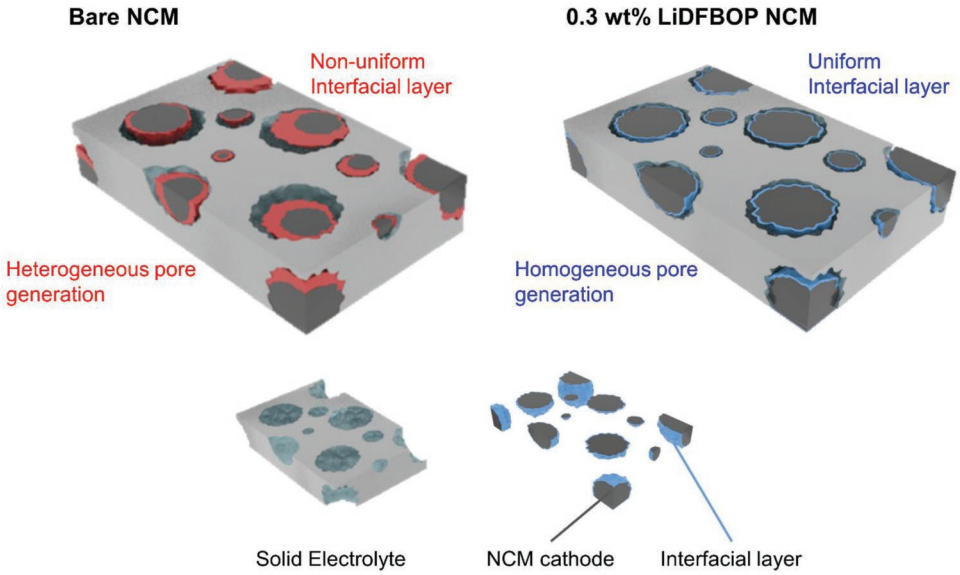

Figure 6. Intertwined chemical-mechanical interface degradation at the cathode interface. Bare NCM suffers kinetically fast chemical degradation and mechanical degradation represented by heterogeneous pore generation. Meanwhile, LiDFBOP-coated NCM exhibits mitigated chemical degradation due to a uniform CEI layer, thus relatively homogeneous pore generation is evolved.

stability in terms of mechanical degradation especially pore size distribution.

3. Conclusion

We proposed the applicability of organic-additive-derived compounds as a new class of cathode coating material for sulfide-based SSBs with dual functionality, simultaneously mitigating chemical and mechanical degradation. Electrochemically oxidized LiDFBOP controlled the kinetics of chemical degradation to be sluggish, resulting in the suppression of solid-electrolyte decomposition. In addition, the LiDFBOP-derived CEI layer was confirmed to contribute to alleviating the pore formation and even maintaining the uniformity of the pore size, resulting in the delivery of high capacity even at low stack pressure below 1 MPa. Consequently, both features of the coating layer enable the achievement of enhanced capacity and retention during long-term cycling even with the application of only a small amount of LiDFBOP. Through systematic post-mortem analysis after battery cycling with and without the coating layer, we discovered that the chemical degradation effect could play a more dominant role in the long-term cycle stability than the mechanical degradation at the cathode-SE interface where the intertwined chemo-mechanical degradation occurs. Our study not only offers a new perspective on the design of cathode coating materials for sulfide-based solid-state batteries using organic-based functional additives beyond conventional-oxide-based inorganic compounds but also provides an in-depth understanding of the cathode–solid electrolyte interfacial degradation of SSBs.

4. Experimental Section

Material Preparation: A sulfide-based argyrodite solid electrolyte, Li_6PS_5Cl (LPSCl), (Inchems Co., Ltd., Korea) and single-crystalline $LiNi_{0.6}Mn_{0.2}Co_{0.2}O_2$ (NCM cathode, BASF) were used for the model study. A mechano-fusion-method-based mechanical powder precursor (Nob-Mini, Hosokawa Micron Co., Ltd., Japan) was used as a dry-milling apparatus. This machine was composed of a cylindrical vessel and a rotator. The horizontal position of the vessel and rotator to position the sample powder downwards from the inner circular wall was the characteristic feature of the milling device, exposing the sample powder to a strong shear force while passing through the gap between the vessel wall and rotor blade (1 mm). The organic additive, LiDFBOP (Chunbo Co., Ltd., Korea), was coated on the NCM via the mechano-fusion coating method with the target amount using the dry-milling apparatus at 2000 rpm for 10 min and 4000 rpm for 30 min.

Cell Assembly and Electrochemical Analysis: The full cells were assembled in an Ar-filled glove box with oxygen and moisture levels below 1 ppm. A model experiment was conducted to confirm the oxidation reaction of the LiDFBOP organic coating layer. The solid-electrolyte composite was prepared by mixing the LPSCl (95 mg) and carbon nanofiber (5 mg) using a mortar and pestle. The additive composite was prepared by mixing the LiDFBOP (65 mg), LPSCl (30 mg), and carbon nanofiber (5 mg) using a mortar and pestle. In the model experiment, 10 mg of the solid-electrolyte composite and 15 mg of the additive composite were used as the active material composite to match the same amount of active material (9.75 mg for the additive composite and 9.5 mg for the solid-electrolyte composite). The pellet for the model experiment was composed of the active-material composite (10 mg for the solid-electrolyte composite and 15 mg for the additive composite), electrolyte layer (150 mg), and Li–In alloy for the composite|SE|In/InLi configuration, filled in a 13-mm-diameter Teflon body, and pressed under 295 MPa for 2 min. Galvanostatic cycling was conducted at a slow current rate of 5.3 μA cm^{-2} in the voltage range of 0.88–4.18 V (vs In/InLi). The cells were fabricated using the argyrodite electrolyte and a cathode to form a cathode composite with a Li–In metal alloy as a counter electrode. The cathode composite was prepared by mixing the active material (65 mg), LPSCl (30 mg), and carbon nanofiber (5 mg) using a mortar and pestle. The pellet for the cell was composed of the cathode composite (15 mg), electrolyte layer (150 mg), and Li–In alloy for an NCM|SE|In/InLi configuration, filled in a 13-mm-diameter Teflon body, and pressed under 295 MPa for 2 min. Then, a constant pressure of 4-Nm torque was applied in the uniaxial direction (stack pressure, ≈13 MPa). Before galvanostatic cycling, the cells were cycled at C/10 for four cycles, and long-term cycling was conducted at C/4 (1 C = 1.32 mA cm^{-2}) at 25 °C in the range of 1.88–3.88 V (vs In/InLi) using a battery measurement system (WBCS 3000, WonATech). To investigate the effect of the LiDFBOP coating on the rate performance, the full cells were cycled at various charge and discharge rates (0.1, 0.2, 0.3, 0.5, 1.0, and 0.1 C).

The resistances of the full cells were evaluated using EIS (Biologic, SP-300). Each EIS data set was divided into HF, MF, and LF based on the frequency range according to the MATLAB code DRTtools,[50] and each frequency denoted the cathode composite ionic resistance, CA|SE interface resistance, and anode|SE interface resistance, respectively. The experimentally measured EIS data was fitted to Z_{DRT} using the following equation:

$$Z_{DRT}(f) = R_{ohm} + \int_0^{\infty} \frac{\gamma(\tau)}{1+i2\pi f\tau} d\tau = R_{ohm} + \int_{-\infty}^{\infty} \frac{\gamma(ln\,\tau)}{1+i2\pi f\tau} d\tau \quad (2)$$

The Gaussian radial basis function and discrete parameters were obtained through regularized regression using the second order regularization derivative and regularization parameters of 10^{-3}.

To elucidate the chemical stability in the presence of the organic coating layer, NCM|SE|In/InLi full cells were charged up to different cut-off voltages of 3.48 and 3.88 V (vs In/InLi) and allowed to rest for 50 h. During the resting time, EIS analysis was performed every 15 min. The impedance spectra were measured by applying a 10-mV amplitude to the open-circuit voltage in the frequency range of 1 MHz to 0.1 Hz. In addition, EIS analysis was performed by changing the capacity in steps of 20 mAh g^{-1} to observe the change in resistance in response to the change in the SOC of the NCM cathode with the LiDFBOP coating layer and 0.75-MPa stack pressure by applying a 10-mV amplitude to the open-circuit voltage in the frequency range of 1 MHz to 0.1 Hz.

Characterization of Solid-State Batteries: The microstructure of the NCM cathode with the LiDFBOP coating was confirmed using scanning electron microscopy (SEM, SU7000, Hitachi) and high-resolution transmission electron microscopy (HR-TEM, JEM-2100F, JEOL). For the cross-sectional SEM and TEM analysis, the samples were prepared using a cooling cross-sectional polisher (CCP, IB-19520CCP, JEOL) and a focused ion beam (FIB, NX2000, Hitachi), respectively. To confirm the presence of the LiDFBOP coating layer, thermogravimetric analysis (TGA) and time-of-flight secondary ion mass spectrometry (TOF-SIMS, TOF-SIMS 5, ION TOF GmbH) surface analysis were performed to confirm the intrinsic properties of the LiDFBOP additive and LiDFBOP coating layer. A pulsed Bi^{3+} ion beam (25 keV) set in high current mode was used for TOF-SIMS surface analysis. Ex situ X-ray photoelectron spectroscopy (XPS, K-Alpha, ThermoFisher) with Al Kα ($h\nu$ = 1486.6 eV) radiation was employed to identify the interfacial chemistry of the NCM cathode. All the XPS spectra were calibrated based on the hydrocarbon peak (284.4 eV). The oxidative degradation product of argyrodite SE was analyzed using solid-state nuclear magnetic resonance (NMR, VNMRS 600, Varian) using a 1.6-mm solid probe after pre-cycling. The operating frequency of ^{7}Li was 233.12 MHz, and measurements were performed on the Hahn echo 1d pulse sequence within the spinning rate of 10 kHz. ^{7}Li NMR spectra were calibrated with respect to 1.0 M LiCl solution. Ex situ X-ray diffraction (XRD, D8 DISCOVERY, Bruker) was performed to

observe the change in volume and lattice parameters as a function of the SOC change of the NCM cathode. XRD analysis was performed on the NCM cathode, which was retrieved from the LIB system using 1 M $LiPF_6$ in mixed carbonate (EC:EMC:DMC = 3:4:3 vol%) electrolyte, for every 20 mAh g^{-1} change in capacity. Mapping the electrode microstructure in 3D was scanned using X-ray computed tomography under accelerating voltage 100 kV, exposure time 3 s, and voxel size 0.65 µm with the true spatial resolution of 500 nm (Zeiss Xradia 620 X-ray microscope, Carl Zeiss, CA, USA). The 3D visualization and analysis (pore size distribution) were used the Dragonfly software.

Supporting Information

Supporting Information is available from the Wiley Online Library or from the author.

Acknowledgements

This work was supported by the Technology Innovation Program (20017836, Inorganic material-based new electrolyte additive for secondary battery) funded by the Ministry of Trade, Industry & Energy (MOTIE, Korea); a National Research Foundation of Korea (NRF) grant funded by the Korea government (MSIT) (No. 2022R1C1C1006575); a National Research Council of Science & Technology (NST) grant by the Korea government (MSIT) (No. CAP21042-000); and the Chunbo Company.

Conflict of Interest

The authors declare no conflict of interest.

Author Contributions

C.P., J.K., and S.-K.J. designed the project and wrote the manuscript. C.P. and J.L. performed the coating synthesis. C.P. and S.L. conducted the structural characterization. Y.J.H. performed the X-ray CT analysis. C.P. performed the electrochemical tests and characterization. J.K. provided constructive advice on the post-mortem analysis and S.-K.J. supervised all aspects of the research.

Data Availability Statement

The data that support the findings of this study are available in the supplementary material of this article.

Keywords

cathode–solid electrolyte interface, chemo-mechanical degradation, electrolyte additives, organic coating layers, oxidative reactions, solid-state batteries

Received: November 14, 2022
Revised: February 13, 2023
Published online: March 9, 2023

[1] M. Armand, J.-M. Tarascon, *Nature* **2008**, *451*, 652.
[2] J. B. Goodenough, Y. Kim, *Chem. Mater.* **2010**, *22*, 587.
[3] J. Janek, W. G. Zeier, *Nat. Energy* **2016**, *1*, 16141.
[4] Y.-K. Sun, *ACS Energy Lett.* **2020**, *5*, 3221.
[5] J. Chen, J. Wu, X. Wang, A. Zhou, Z. Yang, *Energy Storage Mater.* **2021**, *35*, 70.
[6] J. G. Kim, B. Son, S. Mukherjee, N. Schuppert, A. Bates, O. Kwon, M. J. Choi, H. Y. Chung, S. Park, *J. Power Sources* **2015**, *282*, 299.
[7] A. Manthiram, X. Yu, S. Wang, *Nat. Rev. Mater.* **2017**, *2*, 16103.
[8] Z. Zhang, Y. Shao, B. Lotsch, Y.-S. Hu, H. Li, J. Janek, L. F. Nazar, C. -W. Nan, J. Maier, M. Armand, L. Chen, *Energy Environ. Sci.* **2018**, *11*, 1945.
[9] Y. Wang, W. D. Richards, S. P. Ong, L. J. Miara, J. C. Kim, Y. Mo, G. Ceder, *Nat. Mater.* **2015**, *14*, 1026.
[10] A. Banerjee, X. Wang, C. Fang, E. A. Wu, Y. S. Meng, *Chem. Rev.* **2020**, *120*, 6878.
[11] Y. Kato, S. Hori, T. Saito, K. Suzuki, M. Hirayama, A. Mitsui, M. Yonemura, H. Iba, R. Kanno, *Nat. Energy* **2016**, *1*, 16030.
[12] J. C. Bachman, S. Muy, A. Grimaud, H.-H. Chang, N. Pour, S. F. Lux, O. Paschos, F. Maglia, S. Lupart, P. Lamp, L. Giordano, Y. Shao-Horn, *Chem. Rev.* **2016**, *116*, 140.
[13] Y. Zhu, X. He, Y. Mo, *ACS Appl. Mater. Interfaces* **2015**, *7*, 23685.
[14] Y. Zhu, X. He, Y. Mo, *J. Mater. Chem. A* **2016**, *4*, 3253.
[15] S.-K. Jung, H. Gwon, S.-S. Lee, H. Kim, J. C. Lee, J. G. Chung, S. Y. Park, Y. Aihara, D. Im, *J. Mater. Chem. A* **2019**, *7*, 22967.
[16] R. Koerver, I. Aygün, T. Leichtweiß, C. Dietrich, W. Zhang, J. O. Binder, P. Hartmann, W. G. Zeier, J. Janek, *Chem. Mater.* **2017**, *29*, 5574.
[17] W. Zhang, F. H. Richter, S. P. Culver, T. Leichtweiss, J. G. Lozano, C. Dietrich, P. G. Bruce, W. G. Zeier, J. Janek, *ACS Appl. Mater. Interfaces* **2018**, *10*, 22226.
[18] W. Zhang, D. Schröder, T. Arlt, I. Manke, R. Koerver, R. Pinedo, D. A. Weber, J. Sann, W. G. Zeier, J. Janek, *J. Mater. Chem. A* **2017**, *5*, 9929.
[19] J. Haruyama, K. Sodeyama, L. Han, K. Takada, Y. Tateyama, *Chem. Mater.* **2014**, *26*, 4248.
[20] D. H. S. Tan, A. Banerjee, Z. Chen, Y. S. Meng, *Nat. Nanotechnol.* **2020**, *15*, 170.
[21] J. Haruyama, K. Sodeyama, Y. Tateyama, *ACS Appl. Mater. Interfaces* **2017**, *9*, 286.
[22] A. Banerjee, H. Tang, X. Wang, J.-H. Cheng, H. Nguyen, M. Zhang, D. H. S. Tan, T. A. Wynn, E. A. Wu, J. -M. Doux, T. Wu, L. Ma, G. E. Sterbinsky, M. S. D'Souza, S. P. Ong, Y. S. Meng, *ACS Appl. Mater. Interfaces* **2019**, *11*, 43138.
[23] Y. -Q. Zhang, Y. Tian, Y. Xiao, L. J. Miara, Y. Aihara, T. Tsujimura, T. Shi, M. C. Scott, G. Ceder, *Adv. Energy Mater.* **2020**, *10*, 1903778.
[24] Y. Xiao, L. J. Miara, Y. Wang, G. Ceder, *Joule* **2019**, *3*, 1252.
[25] F. Walther, F. Strauss, X. Wu, B. Mogwitz, J. Hertle, J. Sann, M. Rohnke, T. Brezesinski, J. Janek, *Chem. Mater.* **2021**, *33*, 2110.
[26] J. Zhang, H. Zhong, C. Zheng, Y. Xia, C. Liang, H. Huang, Y. Gan, X. Tao, W. Zhang, *J. Power Sources* **2018**, *391*, 73.
[27] S. Ito, S. Fujiki, T. Yamada, Y. Aihara, Y. Park, T. Y. Kim, S.-W. Baek, J.-M. Lee, S. Doo, N. Machida, *J. Power Sources* **2014**, *248*, 943.
[28] W. D. Richards, L. J. Miara, Y. Wang, J. C. Kim, G. Ceder, *Chem. Mater.* **2016**, *28*, 266.
[29] Y.-S. Choi, J.-C. Lee, *J. Power Sources* **2019**, *415*, 189.
[30] S. P. Culver, R. Koerver, W. G. Zeier, J. Janek, *Adv. Energy Mater.* **2019**, *9*, 1900626.
[31] S. S. Zhang, *J. Power Sources* **2006**, *162*, 1379.
[32] K. Xu, *Chem. Rev.* **2014**, *114*, 11503.
[33] B. Liao, H. Li, M. Xu, L. Xing, Y. Liao, X. Ren, W. Fan, L. Yu, K. Xu, W. Li, *Adv. Energy Mater.* **2018**, *8*, 1800802.
[34] H. Ma, D. Hwang, Y. J. Ahn, M.-Y. Lee, S. Kim, Y. Lee, S. -M. Lee, S. K. Kwak, N. -S. Choi, *ACS Appl. Mater. Interfaces* **2020**, *12*, 29365.
[35] Y. Qin, Z. Chen, J. Liu, K. Amine, *Electrochem. Solid-State Lett.* **2010**, *13*, A11.
[36] Z. Chen, Y. Ren, A. N. Jansen, C.-K Lin, W. Weng, K. Amine, *Nat. Commun.* **2013**, *4*, 1513.

[37] S. J. Lee, J.-G. Han, Y. Lee, M.-H. Jeong, W. C. Shin, M. Ue, N.-S. Choi, *Electrochim. Acta* **2014**, *137*, 1.
[38] J. Zheng, M. H. Engelhard, D. Mei, S. Jiao, B. J. Polzin, J.-G. Zhang, W. Xu, *Nat. Energy* **2017**, *2*, 1.
[39] S. H.-S. Cheng, C. Liu, F. Zhu, L. Zhao, R. Fan, C.-Y. Chung, J. Tang, X. Zeng, Y.-B. He, *Nano Energy* **2021**, *80*, 105562.
[40] J. Li, W. Li, Y. You, A. Manthiram, *Adv. Energy Mater.* **2018**, *8*, 1801957.
[41] M. Gruber, A. Leitner, D. Kiener, P. Supancic, R. Bermejo, *Mater. Des.* **2018**, *153*, 221.
[42] H. Shin, J. Park, S. Han, A. M. Sastry, W. Lu, *J. Power Sources* **2015**, *277*, 169.
[43] G. Song, Z. Yi, F. Su, L. Xie, C. Chen, *ACS Appl. Mater. Interfaces* **2021**, *13*, 40042.
[44] C. Park, E. Lee, S. H. Kim, J.-G. Han, C. Hwang, S. H. Joo, K. Baek, S. J. Kang, S. K. Kwak, H.-K. Song, N.-S. Choi, *J. Power Sources* **2022**, *521*, 230923.
[45] J.-G. Han, J. B. Lee, A. Cha, T. K. Lee, W. Cho, S. Chae, S. J. Kang, S. K. Kwak, J. Cho, S. Y. Hong, N.-S. Choi, *Energy Environ. Sci.* **2018**, *11*, 1552.
[46] Y. Zhu, Y. Li, M. Bettge, D. P. Abraham, *Electrochim. Acta* **2013**, *110*, 191.
[47] J.-G. Han, I. Park, J. Cha, S. Park, S. Myeong, W. Cho, S.-S. Kim, S. Y. Hong, J. Cho, N.-S. Choi, *ChemElectroChem* **2017**, *4*, 56.
[48] J. T. S. Irvine, D. C. Sinclair, A. R. West, *Adv. Mater.* **1990**, *2*, 132.
[49] J. Xia, C. Wang, X. Wang, L. Bi, Y. Zhang, *Electrochim. Acta* **2020**, *349*, 136328.
[50] T. H. Wan, M. Saccoccio, C. Chen, F. Ciucci, *Electrochim. Acta* **2015**, *184*, 483.
[51] S. Wenzel, S. Randau, T. Leichtweiß, D. A. Weber, J. Sann, W. G. Zeier, J. Janek, *Chem. Mater.* **2016**, *28*, 2400.
[52] T.-T. Zuo, R. Rueß, R. Pan, F. Walther, M. Rohnke, S. Hori, R. Kanno, D. Schröder, J. Janek, *Nat. Commun.* **2021**, *12*, 6669.
[53] T. K. Schwietert, V. A. Arszelewska, C. Wang, C. Yu, A. Vasileiadis, N. J. J. de Klerk, J. Hageman, T. Hupfer, I. Kerkamm, Y. Xu, E. van der Maas, E. M. Kelder, S. Ganapathy, M. Wagemaker, *Nat. Mater.* **2020**, *19*, 428.
[54] R. Koerver, W. Zhang, L. de Biasi, S. Schweidler, A. O. Kondrakov, S. Kolling, T. Brezesinski, P. Hartmann, W. G. Zeier, J. Janek, *Energy Environ. Sci.* **2018**, *11*, 2142.
[55] P. Minnmann, F. Strauss, A. Bielefeld, R. Ruess, P. Adelhelm, S. Burkhardt, S. L. Dreyer, E. Trevisanello, H. Ehrenberg, T. Brezesinski, F. H. Richter, J. Janek, *Adv. Energy Mater.* **2022**, *12*, 2201425.
[56] J.-M. Doux, H. Nguyen, D. H. S. Tan, A. Banerjee, X. Wang, E. A. Wu, C. Jo, H. Yang, Y. S. Meng, *Adv. Energy Mater.* **2020**, *10*, 1903253.
[57] D. H. S. Tan, Y. S. Meng, J. Jang, *Joule* **2022**, *6*, 1755.
[58] L. Zhou, T.-T. Zuo, C. Y. Kwok, S. Y. Kim, A. Assoud, Q. Zhang, J. Janek, L. F. Nazar, *Nat. Energy* **2022**, *7*, 83.
[59] J. Park, H. Zhao, S. D. Kang, K. Lim, C.-C. Chen, Y.-S. Yu, R. D. Braatz, D. A. Shapiro, J. Hong, M. F. Toney, M. Z. Bazant, W. C. Chueh, *Nat. Mater.* **2021**, *20*, 991.
[60] J. Scharf, M. Chouchane, D. P. Finegan, B. Lu, C. Redquest, M. cheol Kim, W. Yao, A. A. Franco, D. Gostovic, Z. Liu, M. Riccio, F. Zelenka, J. M. Doux, Y. S. Meng, *Nat. Nanotechnol.* **2022**, *17*, 446.
[61] S. Deng, Q. Sun, M. Li, K. Adair, C. Yu, J. Li, W. Li, J. Fu, X. Li, R. Li, Y. Hu, N. Chen, H. Huang, L. Zhang, S. Zhao, S. Lu, X. Sun, *Energy Storage Mater.* **2021**, *35*, 661.
[62] E. Gil-González, L. Ye, Y. Wang, Z. Shadike, Z. Xu, E. Hu, X. Li, *Energy Storage Mater.* **2022**, *45*, 484.
[63] K. G. Naik, D. Chatterjee, P. P. Mukherjee, *ACS Appl. Mater. Interfaces* **2022**, *14*, 45308.